THE ASTROPHYSICAL JOURNAL, 279:896–908, 1984 April 15

GAS DYNAMICS IN THE IMPULSIVE PHASE OF SOLAR FLARES. I. THICK-TARGET HEATING BY NONTHERMAL ELECTRONS

F. NAGAI AND A. GORDON EMSLIE
Department of Physics, The University of Alabama in Huntsville
Received 1983 June 13; accepted 1983 September 9

ABSTRACT

In this paper we investigate numerically the gas dynamical response of the solar atmosphere to a flare energy input in the form of precipitating nonthermal electrons. The origin of these electrons is not addressed; the spectral and temporal characteristics of the injected flux are instead inferred through a thick-target model of hard X-ray bremsstrahlung production. The electrons are assumed to spiral about preexisting magnetic field lines, enabling a one-dimensional spatial treatment to be performed. All electron energy losses are assumed to be due to Coulomb collisions with ambient particles; i.e., we neglect return-current ohmic effects and collective plasma processes. One of the main aims of the study is to contrast our results with earlier work on *conductive* heating of the flare atmosphere; detailed consideration of this issue will be presented in later papers.

The main interesting features we obtain are as follows: A local temperature peak appears at a height of ~ 1500 km above the photosphere. This is due to a spatial maximum in the energy deposition rate from an electron beam; such a feature is not present in conductively heated models. The associated localized high-pressure region drives material both upward and downward. The upward-moving material significantly alters the structure of the overlying corona and creates a hot ($\gtrsim 5 \times 10^7$ K) dense ($\sim 3 \times 10^{10}$ cm^{-3}) region at the loop apex when the pair of upward-propagating hydrodynamic shocks which ascend symmetrically from each leg of the loop collide there. The downward-moving conduction front causes heating down to the depth of the quiet-Sun temperature-minimum region, and further creates a downward-propagating hydrodynamic shock through a piston-like action. If the heating is sufficiently gradual, such as in a flare precursor scenario, a cool ($\sim 50{,}000$ K) dense ($\sim 2 \times 10^{11}$ cm^{-3}) region is formed over an extended height; this may correspond to observed Hα features in limb events.

Subject headings: hydrodynamics — Sun: atmosphere — Sun: flares

I. INTRODUCTION

Solar flares produce bursts of radiation in various wavelengths, from radio through optical and EUV to hard X-rays and even, on occasion, γ-rays (see, e.g., Švestka 1976, 1981; Brown and Smith 1980). The energy ultimately responsible for these emissions is generally accepted to be released through a reconnection of twisted (i.e., nonpotential) magnetic fields high in a solar coronal loop, and much literature has been devoted to modeling the transport of this energy throughout the solar atmosphere, and the ensuing radiation produced. In this paper we shall discuss in some detail the atmospheric response to a beam of high-energy electrons, assumed to be accelerated by electric fields produced in the primary magnetic reconnection process. Although the detailed physics of the production of such electron beams is unclear (see, e.g., Smith 1980), strong evidence in favor of their existence has been adduced from observation of interplanetary electron streams, type III and microwave radio bursts, and, most importantly, hard X-ray emission in flares (see, e.g., Brown and Smith 1980, and references therein). It has been demonstrated (e.g., Kane and Donnelly 1971; Hoyng, Brown, and van Beek 1976; Emslie, Brown, and Donnelly 1978) that the energy in such electron beams is sufficient to energize the chromospheric flare, leading to the concept of the thick-target model (Brown 1971), in which electrons are injected from a point high in the corona downward into the atmosphere, losing their energy by Coulomb collisions (Brown 1972; Emslie 1978) and liberating nonthermal radiation such as gyrosynchrotron microwave (e.g., Kundu and Vlahos 1982) and hard X-ray bremsstrahlung (Brown 1971). In turn, the energized flare plasma leads to enhanced *thermal* emissions in soft X-ray, EUV, and optical wave bands.

It is the aim of this series of papers to interrelate some of these observed manifestations in terms of energy transport in the form of a thick-target electron beam. Most previous modeling of energy transport by such electron beams has assumed that the energy losses are predominantly due to Coulomb collisions with ambient electrons (Brown 1972, 1973*a*; Emslie 1978, 1980, 1981*a*), although some authors (Knight and Sturrock 1977; Shapiro and Knight 1978; Emslie 1980) have also considered the role of reverse-current ohmic losses on the dynamics of the beam (see also Emslie 1981*b*; Brown and Hayward 1982). In addition, much prior literature on thick-target electron energy deposition and the associated atmospheric response has concentrated on *steady state* modeling (Brown 1973*a*; Brown, Canfield, and Robertson 1978) of the low-temperature region of the atmosphere. Some authors (e.g., Kostyuk and Pikel'ner 1975; Somov, Syrovatskii, and Spektor 1981) have considered the time-dependent gas dynamic response of the upper atmosphere to injection of a nonthermal electron beam; however, their treatment of the corona/chromosphere interface as a free surface is somewhat artificial, and their results for parameters in the observationally important solar transition region are not presented in sufficient detail for comparison with observation. In addition, Somov,

Syrovatskii, and Spektor use a highly questionable exponential density versus height structure for their initial model atmosphere. Nagai (1980; see also Wu *et al.* 1981) has carried out a detailed numerical simulation of the gas dynamic response of the entire solar atmosphere; however his calculations assumed the energy input form to be spatially Gaussian, which does not correspond to any currently candidate model for flare energy transport.

In this paper, therefore, we model the full hydrodynamic response of the solar atmosphere, including the chromosphere and the photosphere, to an energy input in the form of a thick-target nonthermal electron beam. In § II we describe the equations used in our analysis. In § III we present the results of our numerical simulations, and in § IV we describe the differences between them and the results of the conductive heating calculations of Nagai (1980). A discussion and summary are presented in § V. Future papers will deal with detailed observational predictions, such as hard X-ray/EUV correlations and the evolution of the hard X-ray spatial structure in the loop.

II. EQUATIONS

The fundamental assumptions and approximations used in our modeling are as follows:

1. The motions of the plasma and the thermal conductive flux are assumed to be one-dimensional (1D) along preexisting uniform magnetic field lines. The 1D assumption is based upon the *a posteriori* result that the gas pressure P in the loop is almost everywhere less than the pressure $B^2/8\pi$ of the surrounding magnetic field $\boldsymbol{B}$ for reasonable field strengths (see, however, Emslie 1981*c*). The assumption of uniform field lines is simply for tractability, especially in the evaluation of the variation of heating rate with depth in the atmosphere (cf. eq. [11] and Emslie [1978]). Allowance for magnetic scattering will lead to different dependences of the heating rate with depth, involving the magnetic field structure in a parametric way (see Leach and Petrosian 1981). We feel that the addition of such free parameters unnecessarily complicates the modeling and obscures the basic hydrodynamic physics involved, and so we adopt a uniform $\boldsymbol{B}$ model. Comparison of Figures 3 and 9 of Leach and Petrosian (1981) shows that this should not result in large discrepancies from a more realistic situation in which $\boldsymbol{B}$ is allowed to vary with position along the loop.

2. The calculations are one-fluid, except allowance is made for the partial ionization fraction of hydrogen in the lower layers of the atmosphere.

3. The loop is assumed to be semicircular with a height of 30,000 km. The energy input is taken to be symmetrical about the loop apex, so that only one-half of the loop need be treated.

4. The electrons are assumed to be injected along untwisted uniform field lines. Scattering and energy loss take place by Coulomb collisions only (i.e., reverse-current ohmic effects are neglected) and are treated in the manner of Emslie (1978), i.e., using a mean scattering treatment. The detailed Fokker-Planck modeling of Leach and Petrosian (1981) supports this approximation for the purposes of bulk heating calculations. Injection of the electrons with a different pitch angle distribution (e.g., isotropic in the downward half-plane) leads to very similar results (see Emslie and Nagai 1984, hereafter Paper II; and Figs. 2, 5, and 6 of Leach and Petrosian 1981).

The fluid equations, in Eulerian form, as as follows (see Nagai 1980):

continuity:

$$\frac{dn}{dt} = -n\frac{\partial v}{\partial x}, \tag{1}$$

momentum:

$$nm_{\rm H}\frac{dv}{dt} = -\frac{\partial P}{\partial x} + nm_{\rm H}g_x + \frac{\partial}{\partial x}\left(\mu\frac{\partial v}{\partial x}\right), \tag{2}$$

energy:

$$nm_{\rm H}\frac{d\epsilon}{dt} = -P\frac{\partial v}{\partial x} + \frac{\partial}{\partial x}\left(\kappa\frac{\partial T}{\partial x}\right) - R + \mu\left(\frac{\partial v}{\partial x}\right)^2 + Q_q(x) + Q_f(x, t), \tag{3}$$

where

$$P = (1 + \beta)nk_{\rm B}T \tag{4}$$

and

$$\epsilon = \frac{1}{\gamma - 1}\frac{P}{nm_{\rm H}} + \frac{\chi}{m_{\rm H}}\beta. \tag{5}$$

In these equations n, v, P, and ϵ are the number density ($\rm cm^{-3}$) of protons plus hydrogen atoms, fluid velocity ($\rm cm\ s^{-1}$), pressure ($\rm dyn\ cm^{-2}$), and internal energy ($\rm ergs\ g^{-1}$) of the plasma; x (in cm) is the distance along the magnetic field lines, measured downward from the loop apex; g_x is the component of the solar gravity along this direction; μ and κ are the viscosity and thermal conductivity coefficients; κ is given by its classical value (Spitzer 1962), except near regions of steep temperature gradient, as discussed below; $m_{\rm H}$ is the hydrogen mass in grams; R is the radiative loss rate per $\rm cm^3$, given by an optically thin expression (e.g., Raymond, Cox, and Smith 1976) in the upper atmosphere and by an approximate optically

thick expression (see Nagai 1980) in the lower levels of the atmosphere; $Q_q(x)$ is the energy input function required to balance the energy losses of the initial model atmosphere, while $Q_f(x, t)$ is the flare energy input function, to be discussed below. The ionization degree β is determined by a modified Saha equation, allowing for departures from local thermodynamic equibrium (see Brown 1973*a*). The quantities k_B and T are Boltzmann's constant and the plasma temperature (K); γ is the ratio of specific heats for an ideal gas, and χ is the ionization potential of hydrogen.

In regions where the temperature gradient $\partial T/\partial x$ becomes very large, the classical formulae for thermal conduction cease to be valid. The maximum thermal flux possible is the saturated flux $(3/2)nm_e v_e^3$, where m_e and v_e are the electron mass and thermal velocity, respectively. When allowance is also made for anomalous flux limitation processes, such as ion-acoustic turbulence (e.g., Smith and Lilliequist 1979), we find that the actual maximum flux possible is somwhat less than this. In the present paper we replace the conductive flux term $\kappa|\partial T/\partial x|$ by the value $0.1nm_e v_e^3$ wherever the former exceeds the latter.

In the solution of equations (1) through (3), there are in general three time scales which must be considered, in order that the numerical method remains stable without accumulation of spurious terms. These are the conduction time scale

$$\tau_C \approx \frac{3nk_B T(\Delta x)^2}{\kappa_0 T^{5/2}\Delta T} \approx 4 \times 10^{-10} \frac{n(\Delta x)^2}{T^{3/2}\Delta T}, \tag{6}$$

the radiation time scale

$$\tau_R \approx \max\left[\frac{3nk_B T}{R(n, T)}\right] \approx 7 \times 10^5 \frac{T}{n} \tag{7}$$

[where we have used an approximate form for an optically thin $R(n, T)$ for $8 \times 10^4 \lesssim 3 \times 10^5$ K—see Raymond, Cox, and Smith 1976], and the disturbance-propagation time scale

$$\tau_D \approx \frac{\Delta x}{c_s + |v|}, \tag{8}$$

where $c_s = (k_B T/m_H)^{1/2}$. In equations (6) and (8), Δx is the mesh size, and ΔT the corresponding temperature increment. Since we treat thermal conduction using a fully implicit scheme, we need not take τ_C into account. Thus the time step for the calculation must satisfy only

$$\Delta t \lesssim \min(\tau_R, \tau_D). \tag{9}$$

This constraint was automatically checked at each time step, and Δt adjusted approximately. The minimum value of τ_R becomes ~ 5 ms at $T \approx 8 \times 10^4$ K, $n \approx 10^{13}$ cm^{-3}, while the minimum value of τ_D has almost the same value when $T \approx 10^6$ K and $\Delta x \approx 2 \times 10^5$ cm.

An initial atmosphere, in energy balance and hydrostatic equilibrium, was constructed as in Nagai (1980). The boundary and initial conditions are also as presented in that paper. This atmosphere determines the form of $Q_q(x)$. As a test of the hydrodynamic code used, we set $Q_f(x, t) = 0$ in equation (3) and $Q_q(x)$ from equation (3) and the initial conditions. The atmospheric structure remained stable for times much greater than the characteristic hydrodynamic time scale, except near the transition region, where small-amplitude fluctuations were created, as a result of the well-known thermal instability which develops in steady state loop models (Antiochos 1979; Oran, Mariska, and Boris 1982; Antiochos *et al.* 1984). These fluctuations are washed out in any heating scenario $[Q(x, t) > 0]$ as a result of the motion of the transition region to a different depth before the fluctuations can significantly develop. The other matter of concern in flare hydrodynamic modeling is the satisfactory resolution of the transition region structure. Since we are not largely concerned with the details of this structure here, we defer discussion of this topic to Paper II, in which the structure of the transition region plays a central role.

In order to compute the flare heating terms $Q_f(x, t)$ we use the collisional analysis of Emslie (1978). Reverse-current ohmic heating terms (Emslie 1980) are neglected since they do not substantially affect the results, especially in the lower regions of the atmosphere (see Emslie 1981*b*; Brown and Hayward 1982). In addition, collective energy losses from the beam (cf. Emslie and Smith 1984) are neglected. We have little rigorous justification for this assumption, especially in light of some recent results (Holman, Kundu, and Papadopoulos 1982). Much work, however, is needed in this area before one can confidently consider such terms. We also note that purely collisional energetics do seem to satisfy the basic requirements of empirical models of the flaring chromosphere (Emslie, Brown, and Machado 1981), somewhat justifying the neglect of other processes.

The relevant equation for our study is equation (34) of Emslie (1978), in which we shall use the values for a fully ionized target, viz., $\beta = 2$ and $\gamma = \Lambda$, the electron-electron Coulomb logarithm, here taken to be 20 (Spitzer 1962). In the lower regions of the atmosphere, the target will in general be only partially ionized, resulting in our model overestimating the heating rate of such levels (Brown 1973*b*; Emslie 1978); however, this error factor ($\lesssim 3$; Brown 1973*b*) is acceptable for the present modeling, bearing in mind the other simplifying assumptions made.

We assume a beam flux spectrum (electrons cm^{-2} s^{-1} per unit E_0) for the injected electrons of the form

$$F(E_0, t) = (\delta - 2)\frac{g(t)}{E_c^2}\left(\frac{E_0}{E_c}\right)^{-\delta}, \qquad E_0 \geq E_c; \tag{10}$$

where $g(t)$ is the energy flux (ergs cm^{-2} s^{-1}) of the beam, and δ is a constant spectral index. The quantity E_c is a low-energy cutoff to the beam, required to make the total energy of the beam finite, which we here take as 15 keV, corresponding to typical values obtained through analysis of break points in observed flare hard X-ray spectra (B. R. Dennis, private communica-

tion). Some authors (e.g., Emslie and Vlahos 1980) have postulated beams with E_c of the order of 100 keV, corresponding to the escaping tail of a hot Maxwellian plasma, the bulk of which is confined to the top of the flare loop. This situation, however, corresponds to a principally "thermal" interpretation of the hard X-ray burst (see, e.g., Emslie and Rust 1979), and so we shall not consider it further in this article. Note also that the representation (10) is a somewhat drastic way of applying the low-energy cutoff, with corresponding consequences for the behavior of the atmosphere—see § III. At this point, however, we shall simply note the artificiality of this form, leaving discussion of smoother cutoffs—see, e.g., Emslie 1980—to where appropriate later in the paper. Since the electrons are assumed to be injected along the field lines, μ_0 (the direction cosine of the injected flux to the magnetic field lines) is unity. With these representations, equation (34) of Emslie (1978) gives the beam energy deposition rate as a function of the traversed particle column number density $N(x, t)[= \int n(x, t)dx; \text{cm}^{-2}]$ as

$$Q_f(x, t) = 2\pi e^4 \Lambda n(x, t)(\delta - 2)g(t)E_c^{\delta - 2} \int_{E^*}^{\infty} (E_0^{-(\delta+1)} dE_0) \Big/ \left[1 - \frac{6\pi e^4 \Lambda N(x, t)}{E_0^2}\right]^{2/3}, \tag{11}$$

where

$$E^* = \max [E_c, (6\pi e^4 \Lambda N)^{1/2}] . \tag{12}$$

Note from equations (10) and (11) that the time dependences of $F(E_0, t)$ and $Q_f(x, t)$ are the same. This is clearly an approximation: the finite travel time of the electrons from their injection site ($x = 0$) to the point x where the heating is considered will modify the time dependence of $Q_f(x, t)$ from the $g(t)$ assumed in equation (11). However, such travel times are, for reasonable loop lengths, $\lesssim 1$ s. Thus, while consideration of electron transit times has an important bearing on the interpretation of short-time scale solar hard X-ray burst features (Emslie 1983), such considerations are unimportant for the understanding of hydrodynamic processes occurring on time scales of tens of seconds, such as considered in this article. To be strictly accurate, we could, of course, *assume* the temporal form of $Q_f(x, t)$ as in eq. (11), implying the time variation of the injected flux $F(E_0, t)$ to be a complicated, energy-dependent function. This is not forbidden by the available hard X-ray data, especially when the electron travel time convolution in *its* signature is allowed for (Emslie 1983). We shall thus proceed on the basis of eq. (11) and adopt simple forms for the $g(t)$ appearing there (see eqs. [22] and [24] below).

If we now define the mean stopping column density for electrons of energy E_c,

$$N_c = \frac{E_c^2}{6\pi e^4 \Lambda}, \tag{13}$$

and a dimensionless column number density parameter,

$$\xi = \frac{N(x, t)}{N_c}, \tag{14}$$

then we obtain the following expressions for $Q_f(x[\xi], t)$:

(*a*) $N = 0$. Equation (11) directly integrates to

$$Q_f(0, t) = 2\pi e^4 \Lambda n \frac{(\delta - 2)}{\delta} \frac{g(t)}{E_c^2} . \tag{15}$$

(*b*) $0 < N \leq N_c$. Making the change of variable $\eta = 6\pi e^4 \Lambda N / E_0^2$ in equation (11) gives

$$Q_f(x, t) = \pi e^4 \Lambda n \frac{(\delta - 2)g(t)}{E_c^2} \xi^{-\delta/2} \int_0^{\xi} \eta^{\delta/2 - 1} (1 - \eta)^{-2/3} d\eta . \tag{16}$$

(*c*) $N \geq N_c$. The same change of variable gives

$$Q_f(x, t) = \pi e^4 \Lambda n \frac{(\delta - 2)g(t)}{E_c^2} B\left(\frac{\delta}{2}, \frac{1}{3}\right) \xi^{-\delta/2} , \tag{17}$$

where B is the beta function (e.g., Abramowitz and Stegun 1965).

Note that the energy deposition rate per particle $[Q_f(x, t)/n]$ has a maximum at $\xi = 1$. We therefore expect a high-pressure region to be formed around $N = N_c = E_c^2/6\pi e^4 \Lambda \approx 10^{17} [E_c \text{ (keV)}]^2 \text{ cm}^{-2}$, and the direction of mass flow to reverse at or around this level. This will be verified by the numerical results of the next section.

In our simulations we will use the values $\delta = 4$ and 6, corresponding (Brown 1971) to hard X-ray bremsstrahlung spectral indices $\gamma = 3$ and 5, respectively. For even integer values of δ, the integral in equation (16) is analytic, and so we derive

$$Q_f(x, t)\Big|_{\delta=4} = 2\pi e^4 \Lambda n \frac{g(t)}{E_c^2} \times \begin{cases} \dfrac{1}{2}, & \xi = 0 ; \\ \dfrac{3}{4\xi^2} [3 - (1 - \xi)^{1/3}(\xi + 3)], & 0 < \xi \leq 1 ; \\ \dfrac{9}{4\xi^2}, & \xi \geq 1 ; \end{cases} \tag{18}$$

and

$$Q_f(x,t)\Big|_{\delta=6} = 4\pi e^4 \Lambda n \frac{g(t)}{E_c^2} \times \begin{cases} \frac{1}{3}, & \xi = 0\ ; \\ \frac{3}{14\xi^3}\left[9 - (1-\xi)^{1/3}(2\xi^2 + 3\xi + 9)\right], & 0 < \xi \le 1\ ; \\ \frac{27}{14\xi^3}, & \xi \ge 1\ . \end{cases} \tag{19}$$

Note that the total energy deposition rates $\int Q_f(x,t)dx$ for $\xi \le 1$ and $\xi \ge 1$ are, respectively, from equations (15)–(17),

$$\int_{0\le\xi\le 1} Q_f(x,t)dx = \left[1 - \frac{1}{3} B\left(\frac{\delta}{2}, \frac{1}{3}\right)\right] g(t)\ , \tag{20}$$

and

$$\int_{\xi\ge 1} Q_f(x,t)dx = \frac{1}{3} B\left(\frac{\delta}{2}, \frac{1}{3}\right) g(t)\ , \tag{21}$$

so that the ratios of heat deposited for $\xi \le 1$ to that deposited for $\xi \ge 1$ are $\frac{1}{3}$ and $\frac{5}{9}$ for $\delta = 4$ and 6, respectively. Physically, this is because of the greater number of more energetic (and so, more penetrating) electrons in harder spectra, and the large difference between these ratios for the two cases leads us to expect somewhat different atmospheric responses in the two cases. We shall discuss this further in § III.

III. RESULTS

We investigate three cases. In the first, case A, we take $\delta = 6$ (see eq. [19]) and $g(t)$ to be relatively small and to vary rapidly on a time scale of the order of seconds. We consider this case as representative of *preflare acceleration*. In case B, we again take $\delta = 6$, but with $g(t)$ in the shape of a triangular pulse of width 60 s and with a relatively energetic maximum. In case C, the time profile of $g(t)$ is the same as for case B, but a harder spectral index, $\delta = 4$ (see eq. [18]), is adopted. In line with the discussion at the end of the previous section, we expect case C to result in a deeper penetration of flare energy. We refer to cases B and C as *flare soft acceleration* and *flare hard acceleration*, respectively.

It should be noted that in all figures to be discussed in this section, the abscissa is *height* (and not length along the loop—this gives the nearly isothermal coronal part of the loop more "shape" on the plots); further, the scale is linear below a height of 2000 km and logarithmic above this value.

a) Case A: Preflare Acceleration

In this scenario, electrons with beam flux spectral index $\delta = 6$ are repeatedly accelerated with a period of 2 s. The shape of the first 2 s pulse is quantitatively given by the triangular form

$$g_A(t) = \begin{cases} 2 \times 10^9 t\ , & 0 \le t \le 1\ ; \\ 4 \times 10^9 - 2 \times 10^9 t\ , & 1 \le t \le 2\ . \end{cases} \tag{22}$$

This pulse shape is repeated for 120 pulses (240 s elapsed time), at which point our calculation is terminated. The heating rate $Q_f(x, t)$ is given by equation (19); the total energy deposited per unit area is

$$E_f = \int_0^{240} g(t)dt = 2.4 \times 10^{11} \text{ ergs cm}^{-2}\ . \tag{23}$$

Figures 1–3 shows the evolution of temperature T, velocity v, and density n, as functions of height h. Each curve is labeled with the appropriate value of elapsed time t (s) since the start of the heating.

As soon as the nonthermal electrons reach the chromosphere, a narrow layer with a local temperature peak appears in the middle chromosphere ($t = 1$ s curve of Fig. 1). This layer has a width of ~30–40 km and is situated ~1500 km above the photosphere ($\tau_{5000\,\text{Å}} = 1$). The temperature in this thin layer reaches $\sim 3.8 \times 10^4$ K, relative to a surrounding temperature of only ~9000 K. This local strong increase in temperature ("chromospheric hot spot") is due to the abrupt cutoff in the injected energy spectrum (eq. [10]); electrons of energy E_c (which carry the most energy per unit E range) are thermalized at just the level of the local peak. Thus this feature should not be taken too literally; smoother forms of low-energy cutoff and/or a broader pitch angle distribution of the injected electrons can even out this feature considerably (see Paper II). However, in all cases we still expect a local maximum in deposited energy around $\xi = 1$, i.e., $N = E_c^2/6\pi e^4\Lambda$ (eq. [13]). This feature will be evident in subsequent scenarios also.

The high pressure created in this region (the density is still relatively close to initial value, the hydrodynamic expansion time being significantly greater than 1 s) causes a flow of material away from this layer in both directions. Thus an upward (negative v) motion dominates over a wide region extending from the loop apex to the upper chromosphere (Fig. 2). As a result, the density in the high-pressure region decreases and that in the surrounding layers is enhanced ($t = 10$ s curve of Fig. 3).

As a result of the repeated energization by the pulse of accelerated electrons, the upper chromospheric material is simultaneously

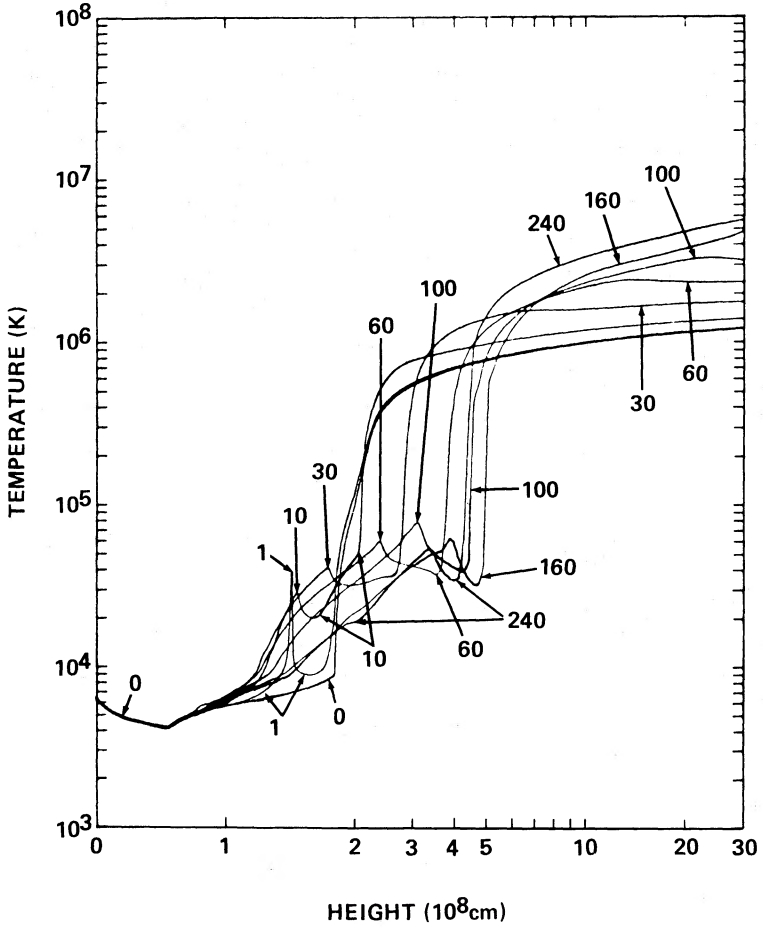

FIG. 1.

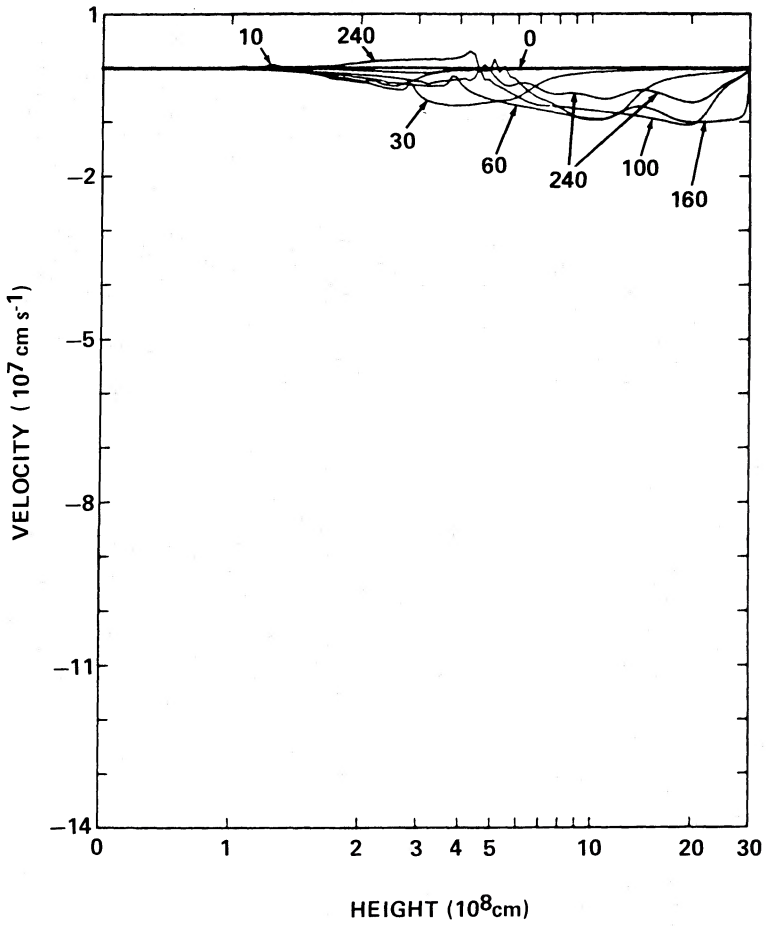

FIG. 2

FIG. 1.—Temperature vs. height for preflare acceleration case A. The curves are labeled with the value of t (s) since the initiation of energy input. Note that an extended region at $T \approx 5 \times 10^4$ K is formed, and that the transition region moves *upward*.

FIG. 2.—Velocity vs. height for case A. Positive velocities are downward.

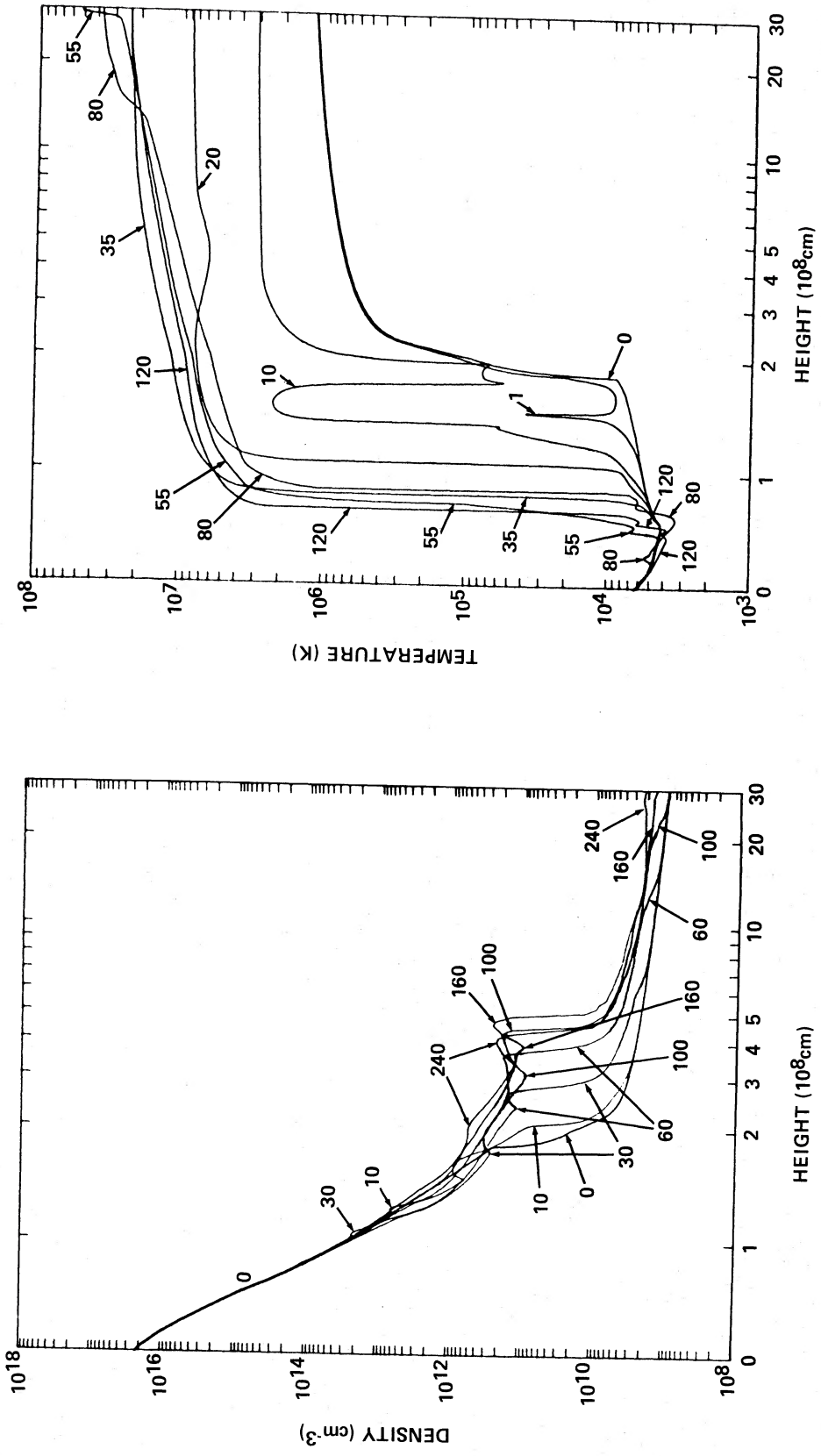

FIG. 3.

FIG. 4.

FIG. 3.—Density vs. height for case A. Note the isochoric region corresponding to the temperature plateau in Fig. 1.

FIG. 4.—Temperature vs. height for flare soft acceleration case B. Note the local temperature maximum for $t = 1$ s, caused by the local spatial maximum in energy deposition rate; this maximum is almost smoothed out by $t = 20$ s. Note also that the transition region moves *downward* with time (cf. Fig. 1), and that a large temperature rise occurs at the loop apex late in the event ($t \approx 55$ s; see § III).

pushed upward and heated. Between $t = 10$ s and 60 s, the cool-temperature ($\sim 50{,}000$ K), high-density ($\sim 2 \times 10^{11}$ cm^{-3}) region stretches into the lower corona, and its ascending front has a speed of 30–40 km s^{-1}. This feature should have a conspicuous signature in low-temperature emissions such as Hα and may correspond to the frequently observed Hα "mound," seen just before or during the initial phase of compact limb events (e.g., Švestka 1976), although heating in many individual loops, much smaller than that considered here, may be necessary in order to reproduce the detailed structure observed in such features. At the same time, the temperature in the corona increases continuously, and the maximum upward motion there approaches 100 km s^{-1}. Thus, the transition region moves to the lower corona and shows a slightly steeper temperature gradient than in the initial atmosphere. On the other hand, the heating in the middle chromosphere gives rise to a descending weak hydrodynamic shock, which creates relatively small increases in plasma density and temperature in deep layers. Because of the inaccurate treatment of the radiative losses in this region, however (see, e.g., McClymont and Canfield 1983), we do not consider it appropriate to discuss these results in detail.

At $t \approx 130$ s, the front of the cool, dense region shows near-zero velocity and reaches its maximum height (~ 5000 km). After this time, the front remains at this height for some time and then recedes slowly. At $t = 240$ s, we can see a downward (positive v) motion of the entire dense region (Fig. 2). This phenomenon is caused by an increase of radiative losses and a corresponding decrease of pressure in the transition region.

b) *Case B: Flare Soft Acceleration*

In this model, we again take $\delta = 6$, but we take $g(t)$ in the form of a 1 minute–wide triangular pulse of significantly greater energy content than case A:

$$g_B(t) = \begin{cases} 2 \times 10^9 t\,, & 0 \le t \le 30 \text{ s}\,; \\ 1.2 \times 10^{11} - 2 \times 10^9 t\,, & 30 \le t \le 60 \text{ s}\,. \end{cases} \tag{24}$$

The total energy injected per unit area is

$$E_f = \int_0^{60} g(t)dt = 1.8 \times 10^{12} \text{ ergs cm}^{-2}\,. \tag{25}$$

We compute quantities only up to $t = 120$ s, since we are primarily interested in the behavior during the impulsive phase. Figures 4–7 show the evolution of the T, P, v, and n profiles throughout the event.

As in case A, the flare energy is deposited mainly in the middle-to-upper chromosphere. Therefore, the temperature in this region rises rapidly, attaining values comparable to those of the corona in 10 s or so (Fig. 4). A region of high gas pressure is formed at this level (Fig. 5), resulting in expulsion of material in both directions. The material in the middle chromosphere is pushed downward, with evaporation from the top surface of this material, while the material in the upper chromosphere expands upward and is rapidly heated (Fig. 6). This in turn leads to a density depression in this region as the atmosphere strives to attain pressure equilibrium (Figs. 5 and 7). On each side of this region local density enhancements are formed as the expelled material presses against the surrounding atmosphere; because the local radiative loss function E (eq. [3]) is proportional to the square of the density, we get a local temperature depression (Fig. 4) at these high-density locations. At $t = 10$ s, a region of cool temperature ($[7\text{–}8] \times 10^4$ K) and high density (5×10^{11}–2×10^{12} cm^{-3}) is formed, surrounded by high-temperature ($[2\text{–}3] \times 10^6$ K), low-density regions in the chromosphere and corona. By $t = 20$ s, however, this cool dense region is further heated, both by direct electron heating and by conduction from the surrounding high-temperature material; it then forms part of the smooth high-temperature corona. At $t = 20$ s, Figure 4 shows a shallow temperature depression at a height of ~ 5000 km, a remnant of the original cool, dense region. The velocity of the ascending front of dense material has now reached ~ 600 km s^{-1} (Fig. 6).

By $t = 35$ s, the great efficiency of thermal conduction in the hot corona has already smoothed out the temperature depression. The ascending high-density front is still present, however, moving at a speed of ~ 1200 km s^{-1} and having reached a height of $\sim 2 \times 10^4$ km. The *downward-moving* conduction front has descended to a height of ~ 800 km, causing heating of material to coronal temperatures and increasing the density in the now evolving flare transition layer (cf. Somov, Syrovatskii, and Spektor 1981). A downward-propagating hydrodynamic shock is generated by the piston-like action of the conduction front, which penetrates deeply into the lower chromosphere. At $t = 55$ s, the density and temperature around the shock have become $\sim 2 \times 10^{15}$ cm^{-3} and 7000 K, respectively.

Since the energy input starts to decrease after $t = 30$ s (eq. [24]), the temperature in the lower corona rises less rapidly and, by $t = 55$ s, has already started to decrease (Fig. 4). However, the temperature and density in the upper corona continue to rise, mainly because of compressional action of the two colliding fronts of ascending material from each footpoint. At $t = 57$ s, the temperature and density at the loop apex have their maximum values of 5.2×10^7 K and 3.5×10^{10} cm^{-3}, respectively.

After $t = 57$ s, a wide region of the upper corona becomes hot and dense, and the velocity of the ascending material decreases rapidly, because of the expansion of the superhot slab (length ≈ 5000 km) formed in the apex region. On the other hand, as the energy input weakens and stops, the large radiative losses around the conduction front lead to the decrease in pressure there. As a result, the downward-propagating shock is forced to diminish rapidly in strength, and, at the same time, the conduction front recedes upward. At $t = 80$ s, temperature and pressure depressions are seen in the lower chromosphere. Then the conduction front moves downward again, and another weak shock is generated (see the $t = 120$ s curve of Fig. 4). As found previously by Nagai (1980), the conduction front recedes slowly upward with a superposed oscillation.

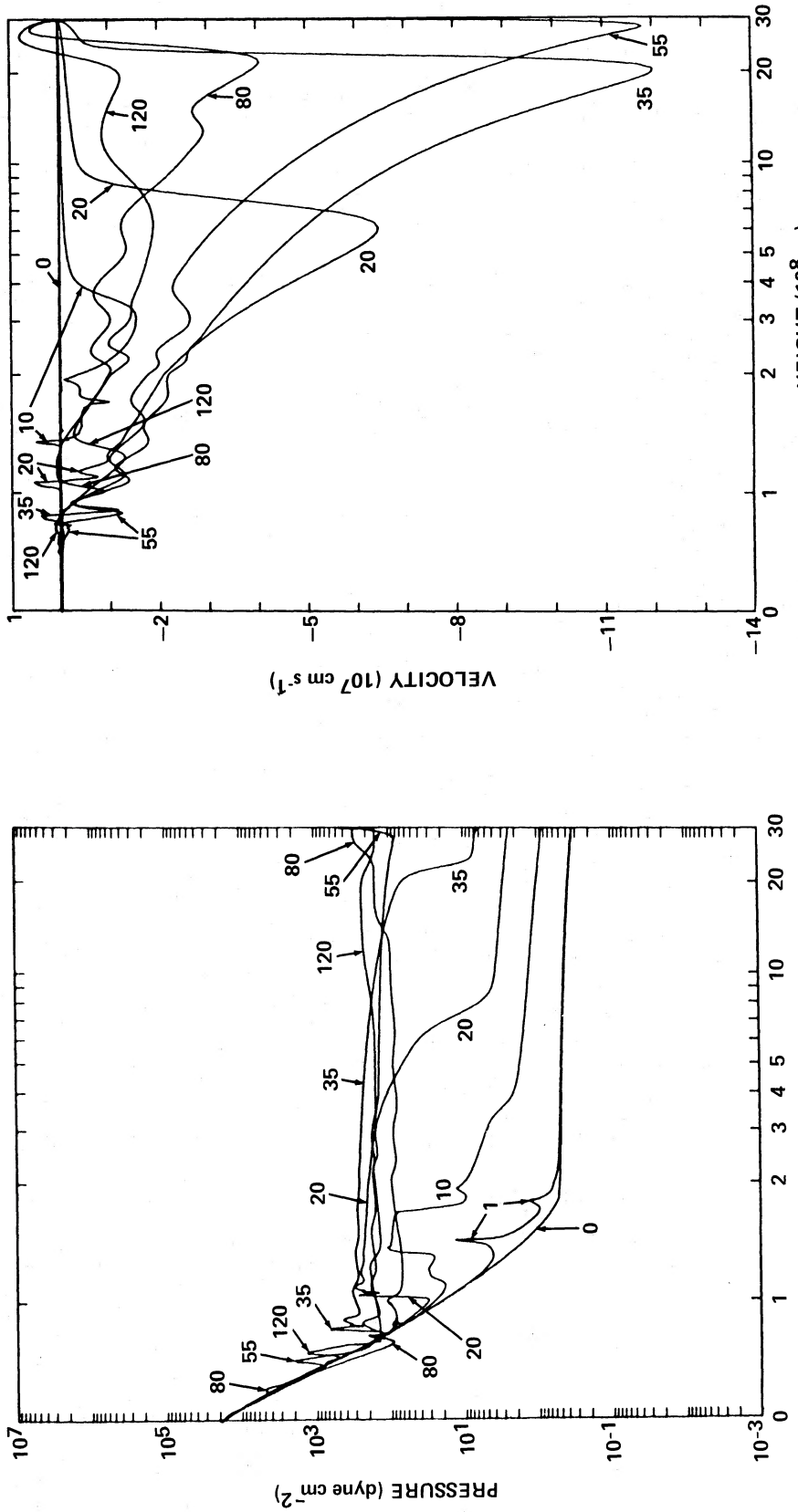

FIG. 6.

FIG. 5.

FIG. 5.—Pressure vs. height for case B. The flaring atmosphere strives for pressure equilibrium, while the deep layers remain in their initial hydrostatic state. Note the double peak in the $t = 1$ s curve (see § IV for discussion) and the large increase in P near the loop apex at $|t \approx 55$ s (e.g., Figs. 4 and 7).

FIG. 6.—Velocity vs. height for case B. The upward-moving density front rapidly accelerates until $t = 50$ s, when it collides with its counterpart from the other leg of the flaring loop, leading to a sudden deceleration, and large density and temperature increases (Figs. 4 and 7).

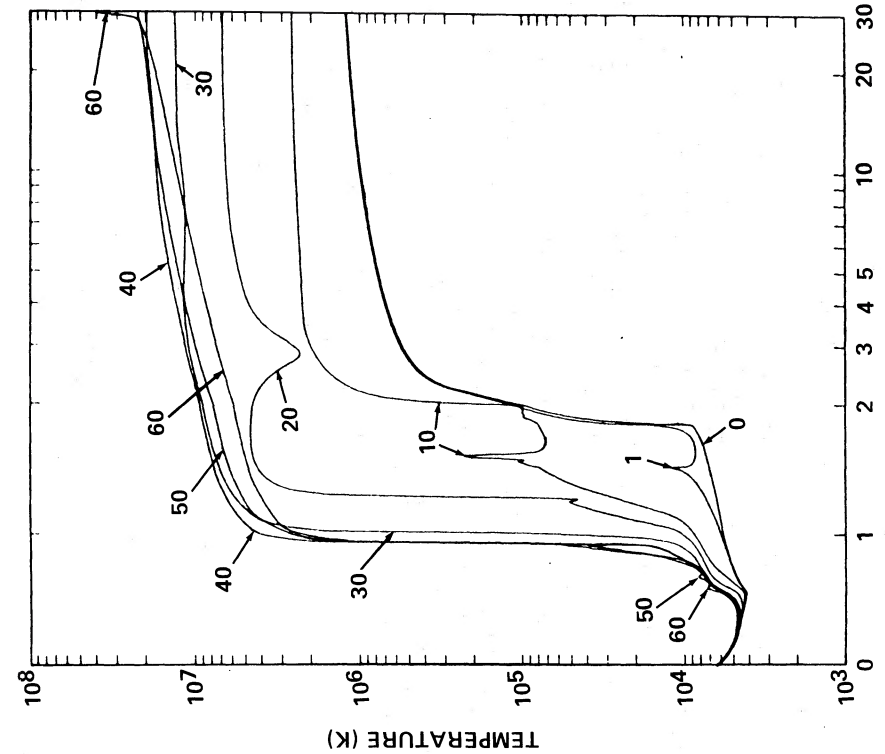

FIG. 8.

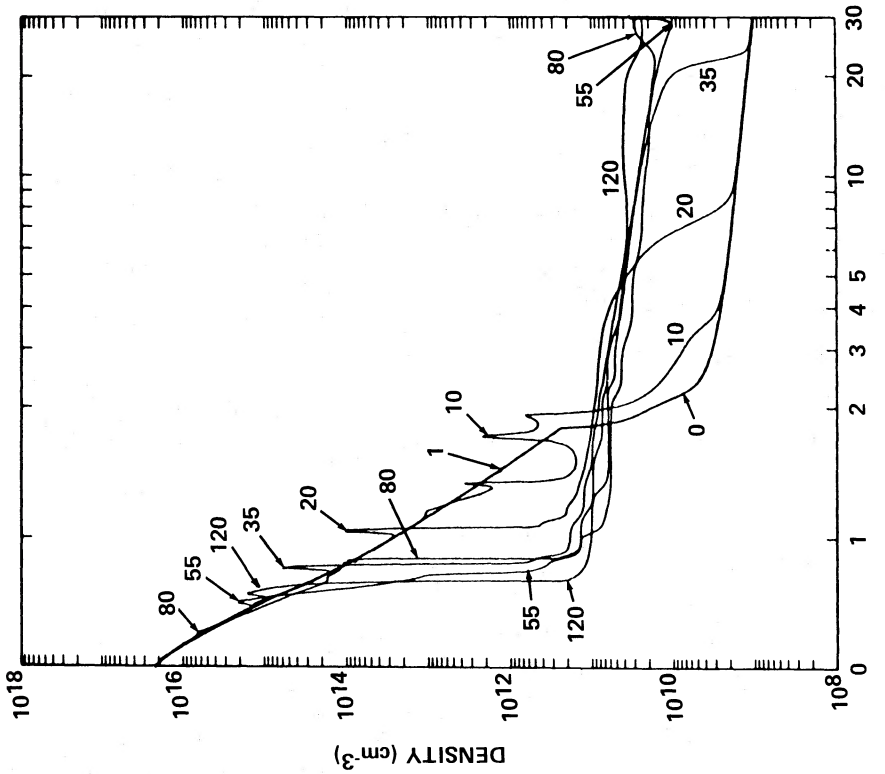

FIG. 7.

FIG. 7.—Density vs. height for case B. Note the detailed structure in the $t = 10$ s curve around 1500 km altitude. The ascending density front reaches the top of the loop at $t \approx 55$ s, leading to a superhot dense region there (e.g., §§ III and V, also Fig. 4).

FIG. 8.—Temperature vs. height for flare acceleration case C. Note the temperature increase in the upper photosphere (300 km $\lesssim h \lesssim$ 550 km); compare with Fig. 4.

c) *Case C: Flare Hard Acceleration*

In case C the variation of $g(t)$ is the same as in case B (see eq. [24]), but the beam flux spectral index $\delta = 4$ (cf. eq. [18]). As noted at the beginning of this section, the harder spectral index leads to a more pronounced heating at deeper levels of the atmosphere than in case B (cf. eqs. [20] and [21]). Figures 8–10 show the behavior of T, v, and n with h for this case. These figures, exhibit the same *qualitative* features as the corresponding figures (4, 6, and 7) for case B; however, there are some *quantitative* differences due to the difference in spatial distribution of deposited energy. Since the bulk of the energy is deposited in the middle-to-low chromospheric region, a large amount of electron energy is used up in the ionization of ambient hydrogen atoms (see § IV for further discussion). Thus, the heating rate of plasma by the downward-moving conduction front is smaller, and the speed of the evaporated material is reduced. As a result, the conduction front does not penetrate as low into the chromosphere as in case B, and the enhancements at the top of the loop created by the collision of the ascending density fronts are less pronounced and occur later in the event.

IV. HEATING BY ELECTRONS IN CONTRAST TO THERMAL CONDUCTION FRONTS

In a previous paper, one of us (Nagai 1980) considered the energization of the solar atmosphere by a descending thermal conduction front, using a hypothetical heat pulse in the apex region of the loop as the energy input source. In the present paper the distribution of heating rate with depth is instead calculated from the dynamics of nonthermal electron beams in an ionized hydrogen target (Emslie 1978). It is therefore of interest to compare our present results with those of Nagai (1980). In a later paper (Paper II) we will pursue this comparison on a more quantitative basis, with particular emphasis on the transition region response to the flare energy input.

The basic physical difference between the two heating scenarios is the presence, in the electron-heated case, of a local maximum in the energy input rate. This feature is absent in the conductively heated model, where the original energy input was assumed to decrease montonically with depth. The main characteristic resulting from this local maximum in the energy deposition rate is the *upward* motion of material away from the resulting region of high gas pressure in the impulsive phase.

The local maximum in energy input gives rise, as expected, to a local maximum in the plasma temperature there. However, Figure 5 shows that the pressure distribution has a *double* peak at $t = 1$ s. A single peak would correspond, naturally enough, to the above temperature maximum. The explanation for the other is that the increase in gas pressure is suppressed in the chromosphere because of the energy required to ionize the ambient neutral hydrogen atoms. If we neglect the change of number density, the ratio ζ of the energy consumed for ionization to that for increase in pressure is obtained by using the modified Saha equation (see Brown 1973*a*) as follows:

$$\zeta \approx \frac{\beta(1-\beta)}{(1+\beta)(2-\beta)} \approx \frac{51405 \ln 10}{T} \approx \frac{1.6 \times 10^5}{T} . \tag{26}$$

Roughly speaking, in a region where $0.1 \lesssim \beta \lesssim 0.9$, i.e., around 7,000 K $\lesssim T \lesssim$ 10,000 K in our model, ζ becomes much larger than unity. This region of reduced pressure enhancement leads to the double-peaked structure of Figure 5. The smaller peak of the pair produces transient *downward* motion at a thin ($\sim$70 km) layer in the upper chromosphere; however, this transient effect is short lived ($t \lesssim 3$ s), and the upward motion away from the location of energy input maximum soon dominates.

In the conduction-heated model of Nagai (1980), the energy was assumed to be input with a Gaussian spatial form, centered about the loop apex. This naturally led to a Gaussian pressure distribution in the initial stages of the heating and a downward motion of material away from the pressure maximum at the top of the loop. Only when this downward-moving conduction front reached the chromosphere was any upward motion seen. Thereafter, the two models—electron- and conduction-heated—behave in a qualitatively similar manner, since thermal conduction efficiently transports any energy released in the corona down to the conduction front, where it is deposited at depths roughly the same as the collisional stopping depth of nonthermal electrons.

Finally, in the electron-heated model, especially with hard spectral index δ (case C), some part of the flare energy can penetrate directly into deep layers, passing through the conduction front en route. On the other hand, in the conduction-heated model, this cannot happen. Instead, a *stronger* downward-propagating shock is generated than in the electron-heated model, which transports the flare energy into the deep layers of the atmosphere.

V. SUMMARY AND DISCUSSION

We have investigated the macroscopic hydrodynamic effects of injection of a beam of energetic nonthermal electrons into a flare loop, assuming that the electrons lose all of their energy through Coulomb collisions alone. For moderate energy input rates (the preflare acceleration case A) we find that the atmosphere slowly evolves to a state with a coronal temperature of $\sim 5 \times 10^6$ K, the temperature enhancements persisting down to around the 5000 K level of the lower chromosphere. More significantly, a fairly extensive region of $\sim$50,000 K plasma with a density of $\sim 2 \times 10^{11}$ cm^{-3} is produced, possibly corresponding observationally to limb formations in Hα light (e.g., Švestka 1976). For stronger energy input rates (cases B and C), both upward- and downward-moving hydrodynamic shocks are generated, because of the local maximum in the energy deposition rate versus depth function for the case of electron heating (see § II). In all three cases considered, the upward motion persists over a wide region extending from the upper chromosphere to the loop apex. This contrasts with the earlier work on *conduction* heating (e.g., Nagai 1980), in which upward-motions are produced only when the downward-moving conduction front impinges on the chromosphere.

The density fronts ascend toward the loop apex from both legs of the loop. When these collide, large increases in density and

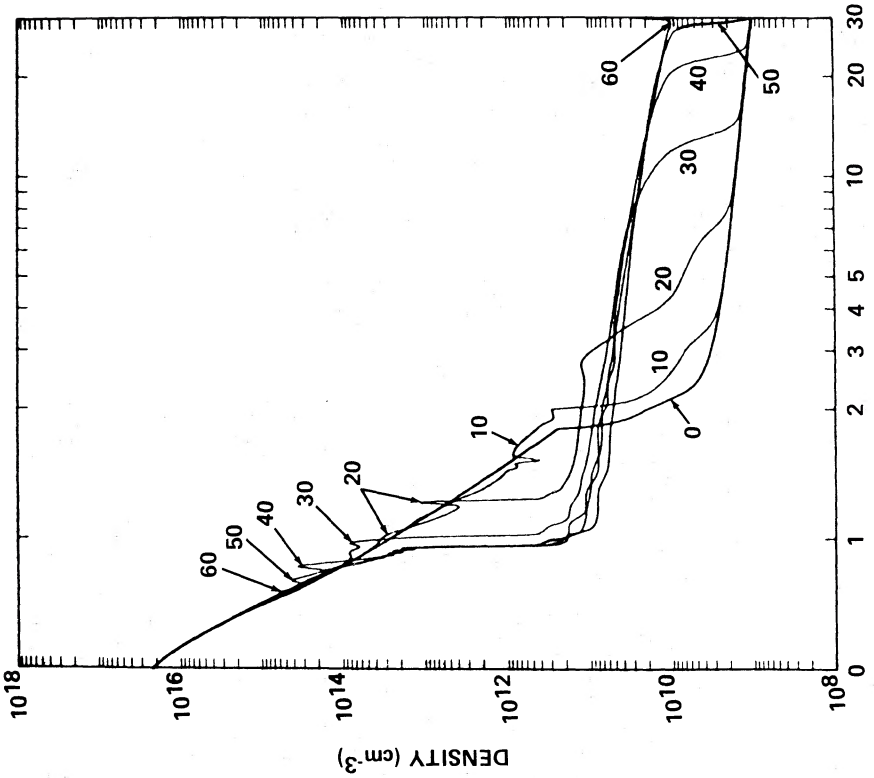

FIG. 10.—Density vs. height for case C. Compare with Fig. 7.

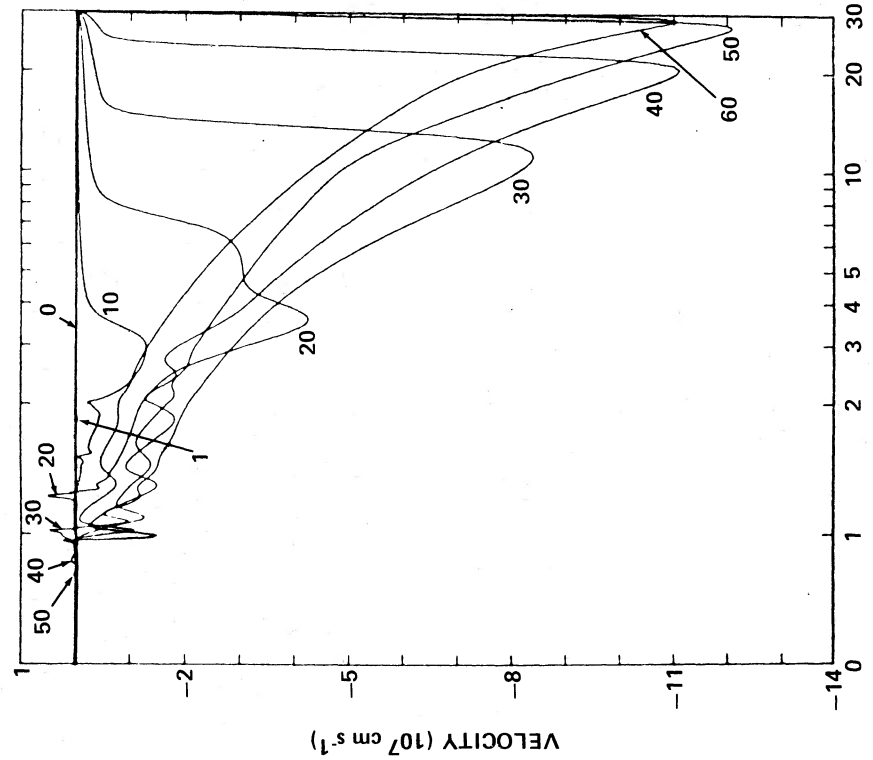

FIG. 9.—Velocity vs. height for case C. Compare with Fig. 6.

temperature result. Such a region could provide a significant contribution to the hard X-ray flux in some events; indeed, there are some observations (Ohki *et al.* 1982; Tsuneta *et al.* 1983) of events in which the dominant hard X-ray contribution appears to come from just such a region at the top of a flaring loop. However, our detailed calculations are somewhat artificial in this area, since they assume perfect symmetry about the loop apex; any asymmetry will cause a difference in front strengths and velocities which will affect the position, temperature, and density (and possibly velocity) of the hard X-ray emitting region. Since it is indeed likely that significant asymmetries do exist in flare loops, we shall not pursue this matter further at the present time.

It is clear that significant advances in our understanding of flare energy transport may be made by a detailed comparison of our model with observations; we leave this to future study. For example, we would ideally like to use a form for $g(t)$ and $\delta(t)$ prescribed by thick-target modeling of a given hard X-ray event and then compare emission measures, etc., predicted by the model with those deduced empirically by spectroscopic analysis. A suitable event for such a study is the 1980 November 5 event ($\sim$2335 UT), for which hard X-ray, soft X-ray line and continuum, Fe XXI and O V EUV lines, Hα, and other morphological data exist—work in this area is currently in progress. Further, detailed comparison of the predictions of conduction- versus electron-heated models may permit observational discrimination between the two heating scenarios. We are at present carrying out such an analysis with emphasis on O V line intensity versus time profiles (cf. Poland *et al.* 1982); the results of this work will form Paper II of this series.

This work was supported by NASA grant NAGW-294 and NSF grant ATM-8200934. During the course of the research, A. G. E. held a von Braun Fellowship at UAH. F. N. was supported by an NRC Postdoctoral Fellowship at NASA/Marshall Space Flight Center during the early stages of this work, and he extends his thanks to Drs. E. Tandberg-Hanssen and E. Hildner and the rest of the Solar Physics Branch there. We thank Dr. L. Vlahos for his helpful comments on an earlier version of the manuscript.

REFERENCES

Abramowitz, M., and Stegun, I. A., eds. 1965, *Handbook of Mathematical Functions* (Washington, D.C.: National Bureau of Standards).
Antiochos, S. K. 1979, *Ap. J. (Letters)*, **232**, L125.
Antiochos, S. K., Emslie, A. G., Shoub, E. C., and An, C.H. 1984, *Ap. J.*, submitted.
Brown, J. C. 1971, *Solar Phys.*, **18**, 489.
———. 1972, *Solar Phys.*, **26**, 441.
———. 1973*a*, *Solar Phys.*, **31**, 143.
———. 1973*b*, *Solar Phys.*, **28**, 151.
Brown, J. C., Canfield, R. C., and Robertson, M. N. 1978, *Solar Phys.*, **57**, 399.
Brown, J. C., and Hayward, J. 1982, *Solar Phys.*, **80**, 129.
Brown, J. C., and Smith, D. F. 1980, *Rept. Progr. Phys.*, **43**, 125.
Emslie, A. G. 1978, *Ap. J.*, **224**, 241.
———. 1980, *Ap. J.*, **235**, 1055.
———. 1981*a*, *Ap. J.*, **245**, 711.
———. 1981*b*, *Ap. J.*, **249**, 817.
———. 1981*c*, *Ap. Letters*, **22**, 171.
———. 1983, *Ap. J.*, **271**, 367.
Emslie, A. G., Brown, J. C., and Donnelly, R. F. 1978, *Solar Phys.*, **57**, 175.
Emslie, A. G., Brown, J. C., and Machado, M. E. 1981, *Ap. J.*, **246**, 337.
Emslie, A. G., and Nagai, F. 1984, in preparation (Paper II).
Emslie, A. G., and Rust, D. M. 1979, *Solar Phys.*, **65**, 271.
Emslie, A. G., and Smith, D. F. 1984, *Ap. J.*, **279**, 882.
Emslie, A. G., and Vlahos, L. 1980, *Ap. J.*, **242**, 359.
Holman, G. D., Kundu, M. R., and Papadopoulos, K. 1982, *Ap. J.*, **257**, 354.
Hoyng, P., Brown, J. C., and van Beek, H. F. 1976, *Solar Phys.*, **48**, 197.
Kane, S. R., and Donnelly, R. F. 1971, *Ap. J.*, **164**, 151.
Knight, J. W., and Sturrock, P. A. 1977, *Ap. J.*, **218**, 306.
Kostyuk, N. D., and Pikel'ner, S. B. 1975, *Soviet Astr.*, **18**, 590.
Kundu, M. R., and Vlahos, L. 1982, *Space Sci. Rev.*, **32**, 405.
Leach, J., and Petrosian, V. 1981, *Ap. J.*, **251**, 781.
McClymont, A. N., and Canfield, R. C. 1983, *Ap. J.*, **265**, 483.
Nagai, F. 1980, *Solar Phys.*, **68**, 351.
Ohki, K., *et al.* 1982, in *Hinotori Symposium on Solar Flares* (Tokyo: Institute of Space and Astronautical Science), p. 102.
Oran, E. S., Mariska, J. T., and Boris, J. P. 1982, *Ap. J.*, **254**, 349.
Poland, A. I., *et al.* 1982, *Solar Phys.*, **78**, 201.
Raymond, J. C., Cox, D. P., and Smith, B. W. 1976, *Ap. J.*, **204**, 290.
Shapiro, P. R., and Knight, J. W. 1978, *Ap. J.*, **224**, 1028.
Smith, D. F. 1980, *Solar Phys.*, **66**, 135.
Smith, D. F., and Lilliequist, C. G. 1979, *Ap. J.*, **232**, 582.
Somov, B. V., Syrovatskii, S. I., and Spektor, A. R. 1981, *Solar Phys.*, **73**, 145.
Spitzer, L. W. 1962, *Physics of Fully Ionized Gases* (2d ed.; New York: Interscience).
Švestka, Z. 1976, *Solar Flares* (Dordrecht: Reidel).
———. 1981, in *Solar Flare Magnetohydrodynamics*, ed. E. R. Priest (New York: Gordon and Breach), p. 47.
Tsuneta, S., *et al.* 1983, *Solar Phys.*, **86**, 313.
Wu, S. T., Kan, L. C., Nakagawa, Y., and Tandberg-Hanssen, E. A. 1981, *Solar Phys.*, **70**, 137.

A. Gordon Emslie: Department of Physics, UAH, Huntsville, AL 35899

Fukuo Nagai: Department of Theoretical Physics, Oxford University, 1 Keble Road, Oxford OX1 3NP, England, UK